
Article:
Jones, B., Lio, W.H. and Rossiter, J. (2018) Overcoming fundamental limitations of wind turbine individual blade pitch control with inflow sensors. Wind Energy, 21 (10). pp. 922-936. ISSN: 1095-4244

https://doi.org/10.1002/we.2205

WIND ENERGY
Wind Energ. 2013; **00**:1–16
DOI: 10.1002/we

RESEARCH ARTICLE

Overcoming fundamental limitations of wind turbine individual blade pitch control with inflow sensors

B. Ll. Jones[1], W. H. Lio[1], J. A. Rossiter[1]

[1]Department of Automatic Control and Systems Engineering, The University of Sheffield, Sheffield, S1 3JD, UK.

ABSTRACT

Individual pitch control (IPC) provides an important means of attenuating harmful fatigue and extreme loads upon the load bearing structures of a wind turbine. Conventional IPC architectures determine the additional pitch demand signals required for load mitigation in response to measurements of the flap-wise blade-root bending moments. However, the performance of such architectures is fundamentally limited by bandwidth constraints imposed by the blade dynamics. Seeking to overcome this problem, we present a simple solution based upon a local blade inflow measurement on each blade. Importantly, this extra measurement enables the implementation of an additional cascaded feedback controller that overcomes the existing IPC performance limitation and hence yields significantly improved load reductions. Numerical demonstration upon a high-fidelity and nonlinear wind turbine model reveals (i) 60% reduction in the amplitude of the dominant 1P fatigue loads, and (ii) 59% reduction in the amplitude of extreme wind shear induced blade loads, compared to a conventional IPC controller with the same robust stability margin. This paper therefore represents a significant alternative to wind turbine IPC load mitigation as compared to LiDAR-based feedforward control approaches. Copyright © 2013 John Wiley & Sons, Ltd.

KEYWORDS

Individual pitch control; load reduction; cascaded control; blade inflow measurement

Correspondence
B. Ll. Jones, Department of of Automatic Control and Systems Engineering, The University of Sheffield, S1 3JD, UK.
E-mail: b.l.jones@sheffield.ac.uk

Received . . .

1. INTRODUCTION

The worldwide growth of offshore wind farms places increasing importance on reliable operation to minimise the need for costly maintenance and repair activity. Technologies that can reduce such activity are thus of significant importance. Principal amongst these is the use of individual pitch control (IPC) [1, 2, 3] as a means of mitigating the harmful loads that arise from spatially uneven and temporally unsteady winds, primarily in above rated conditions. Conventional IPCs actuate the motors at the roots of each blade to individually adjust the blade pitch angles, in response to measurements of the flap-wise blade root bending moments. Such pitch angle adjustments are in addition to those set by the collective pitch controller (CPC), whose primary objective is to maintain the rated rotor speed.

Numerous IPC studies have been conducted in recent years, employing various architectures (e.g. individual blade pitch control [4], Coleman Transform-based IPC [5]) and different controller design methodologies (e.g. PI [6], LQR [7], LQG [8], predictive repetitive [9], $\mathcal{H}_\infty$ loop-shaping [10]). Successful experimental demonstrations have also been performed [11]. These studies have all shown significant reductions in blade fatigue loads, particularly with respect to the dominant once-per-revolution (1P) loads [2]. Upon the non-rotating turbine structures, the main fatigue loads occur at 3P frequencies, corresponding to 2P and 4P loads in the rotating frame of reference [10]. These are more challenging to attenuate given the necessity for higher controller bandwidth, which is difficult to achieve with conventional IPC. The use of flap-wise root bending moment sensors gives rise to significant measurement lag, since disturbance loads are only detected once the blade has undergone distortion. Once this load is detected, the entire blade must then be rotated to

mitigate the disturbance, by which time it may no longer be present. This has motivated a large body of research into improved load mitigation, which can broadly be divided into the following areas:

1.1. Improved controller design

As mentioned above, numerous studies have considered the controller design aspects of IPC, both from methodological and architectural perspectives. In terms of the former, since feedback controller design is heavily dictated by the plant dynamics and control objectives, any well designed IPC should perform well irrespective of the particular methodology employed. From an architectural perspective, IPC design in recent years has split into two branches characterised by the targeted loads. The first branch targets loads upon the non-rotating turbine structures and employs the Coleman Transform to project signals from the rotating frame of reference, to the fixed (e.g. [4, 6, 12, 13, 14, 10]). The second branch targets load reductions upon the rotating blades and is commonly referred to as single-blade or individual-blade control (e.g. [15, 16]), whereby each blade is equipped with its own controller. Importantly, the issue of which architecture leads to the best performance in terms of load reductions was recently resolved in [17], where it was shown that IPC controllers can be designed using either architecture to give exactly the same performance. Hence, there is little scope to improve conventional IPC performance from a purely feedback control design perspective. Augmentation of conventional IPC with additional feedforward/feeback control can improve performance, but these strategies typically rely upon the provision of extra information from additional sensors, which will be discussed in further detail below.

1.2. Improved blade design

With little additional benefit to be leveraged from the IPC controller, the only option is to redesign the physical hardware, consisting of actuators, blades and sensors. As will be explained in Section 2, the bandwidth limitation of conventional IPCs is imposed by the blade dynamics, and so advances in materials and blade design offer potential performance improvements. One particularly promising concept is that of aeroelastically tailored composite blades [18], wherein the lay-up and thicknesses of the composite layers is tailored to enable blade-twist coupling [19] that induces twisting in response to flap-wise bending. In such case, the blade functions as a passive closed-loop system, passively deforming in response to wind disturbances so as to mitigate undesirable loads. To what extent this can mitigate loads across a range of operating conditions, whilst simultaneously maintaining aerodynamic performance, remains to be seen. Additionally, issues relating to repeatability of manufacture will likely lead to dynamic variation between blades, and so we speculate that aeroelastic tailoring will compliment, rather than replace IPC, by reducing the burden on the pitch actuator.

1.3. Improved actuation

There has been considerable recent research activity in the use of distributed actuators upon wind turbines blades, leading to the the concept of the so-called ‘smart rotor’ [20]. Such actuators are designed to provide localised control of the aerodynamic forces, and are capable of faster actuation than blade-pitch control owing to their smaller size and inertia. Devices under study have included trailing edge flaps [13, 21], microtabs [22], plasma actuators [23] and synthetic-jet actuators [24]. In [14], a smart rotor consisting of distributed trailing edge flaps was augmented to an existing IPC to investigate the additional benefits. For a given performance with respect to load reductions, the augmented smart rotor placed lower demands upon the pitch actuator in terms of travel, rates and power requirements. However, the authors concluded these benefits alone made it difficult to justify the added design complexities of a smart rotor, as opposed to upgrading the pitch actuator and bearing.

1.4. Improved sensing

The use of different sensors can enable earlier/faster detection of blade loads than is possible with blade-root bending moment sensors, offering a potential means of improved IPC performance. Faster detection enables design of feedback loops with higher bandwidth owing to a reduction in sensor lag, whilst earlier detection affords the design of feedforward controllers that can initiate mitigating pitch actuation in advance. A review of load monitoring sensors for active control of wind turbines appears in [25]. Of particular interest to this study are the use of local aerodynamic sensors, such as pitot-static tubes.

Pitot-static tubes can provide measurements of the local angle of attack and relative wind speed. Such measurements may be introduced into IPC schemes in various ways [26]. For example, using measurements taken at three-quarters of the rotor radius, an angle-of-attack feedback controller was combined with a relative velocity-based feedforward controller to yield an IPC that reduced 20 year fatigue loads by 25% over a traditional CPC [26]. In a further study [27], local inflow measurements were used to determine the blade-root moments from the free-stream velocity. This enabled the design of an IPC controller with a feedforward component from inferred future loads, leading to significant reduction in magnitudes of the tilt and yaw moments. As with any sensor technology, there are issues of reliability concerning the use of pitot-static

Wind Energ. 2013; **00**:1–16 © 2013 John Wiley & Sons, Ltd.
DOI: 10.1002/we
Prepared using weauth.cls

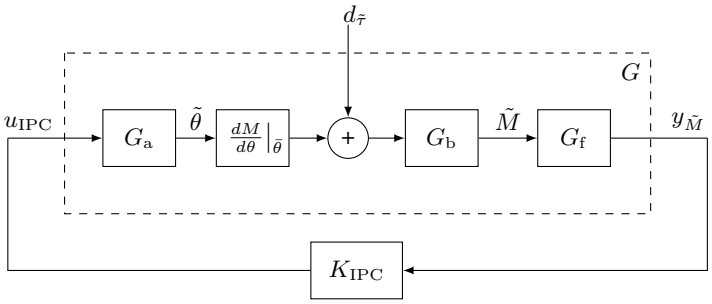

Figure 1. Single blade IPC system diagram, consisting of blade G and IPC controller K_{IPC}. All terms are defined in Section 2.

tubes (e.g. blockage), but experimental campaigns [28] have demonstrated the ability of these sensors to detect inflow disturbances of importance in the design IPCs.

Despite the promise of the use of inflow blade measurements, the number of studies exploring this technology has become heavily outnumbered in recent years in favour of remote inflow sensors, such as LiDAR (e.g. [29, 30, 31], [32] and references therein). According to [33] LiDAR sensors are regarded as suitable for mean wind speed assessment, but suffer from some issues that hinder the measurement of gusts (and hence the development of IPC controllers). Amongst these is the difficulty of disambiguating wind speeds and directions [34] and the fact that LiDAR assisted control is feedforward, meaning that performance is sensitive to the accuracy of the inflow model linking upstream flow measurements to future blade loads. Accurate models are described by the atmospheric boundary layer equations [35], but such models are too complex for real-time control purposes and so any LiDAR-based feedforward control scheme will require simplifying assumptions concerning the flow. Hence, the validity of any simulation-based study of LiDAR-based feedforward control must be assessed against the physical accuracy of the associated wind-field models. In terms of experimental studies of LiDAR assisted control, most have focussed on improving rotor speed regulation via improved CPC design, rather than the more complex IPC problem. Of the few studies that have compared IPC performance using local inflow and blade measurements versus LiDAR, it was shown in [36] that poorer 1P load rejection was achieved from LiDAR-based cyclic pitch schemes under conditions of turbulent inflow, for reasons relating to the accuracy of the model employed in the feedforward controller.

Motivated by the problems associated with LiDAR-assisted control, the aim of this paper is to show that the performance of conventional IPC can be significantly improved in a far less complex fashion. The contributions of this paper are twofold;

- Firstly, to explain a fundamental limitation of traditional IPC schemes from a control-theoretic perspective.
- Secondly, to demonstrate how this limitation can be overcome with an additional, cascaded *feedback* controller based upon a single extra inflow measurement on each blade. In particular, the fashion in which the inflow sensor is employed is novel, as is the resulting IPC architecture.

The remainder of this paper is organised as follows. In Section 2 we discuss the performance limitations of existing IPC architectures. In Section 3, we show how this limitation can be overcome via a cascaded control architecture that uses an extra measurement from a local blade inflow sensor, and show how such a measurement can be obtained from a pitot-static tube. In Section 4, a cascaded and conventional IPC controller are designed, and their relative performances assessed via closed-loop simulation. Finally, Section 5 presents the conclusions of this paper.

2. PERFORMANCE LIMITATION OF EXISTING IPC ARCHITECTURES

We begin by considering the single-blade formulation of an IPC controller, shown in Figure 1. The single-blade formulation is chosen for simplicity, but the results in this paper extend to fixed frame of reference IPCs, owing to the performance equivalence results established in [17]. The single blade model is represented by a transfer function $G(s) \in \mathcal{R}$, where s is a complex variable and $\mathcal{R}$ is the space of real-rational transfer functions with one input and one output. This transfer function relates the IPC blade pitch-angle input u_{IPC} to the measurement $y_{\tilde{M}}$ of the perturbation flap-wise bending moments $\tilde{M}$ at the blade root. The system is perturbed by a lumped wind-induced flap-wise disturbance torque $d_{\tilde{\tau}}$ acting upon the blade. Here, perturbations are defined as the difference between a signal and its time averaged value, for example:

$$\tilde{M}(t) := M(t) - \bar{M},$$

Parameter	Value	Units	Description
τ	0.11	sec	Pitch actuator time constant
$\frac{dM}{d\theta}\big\vert_{\bar{\theta}}$	1.50×10^6	Nm/deg	Variation of blade flap-wise bending moment with respect to pitch angle
ω_{flap}	4.21	rad/s	Natural frequency of first blade flap-wise mode
ω_{edge}	6.79	rad/s	Natural frequency of first blade edge-wise mode
ζ_{b}	0.48	-	Blade aerodynamic damping ratio
ω_{h}	19.73	rad/s	Bandpass filter high corner frequency
ω_{l}	0.088	rad/s	Bandpass filter low corner frequency

Table I. Model parameters of $G(s)$ (1).

where $\bar{M}$ denotes the mean value. A low-order model of the blade system is as follows:

$$G(s) := G_{\mathrm{f}}(s)G_{\mathrm{b}}(s)\left.\frac{dM}{d\theta}\right|_{\bar{\theta}} G_{\mathrm{a}}(s), \tag{1a}$$

where $(dM/d\theta)|_{\bar{\theta}} \in \mathbb{R}$ is the sensitivity of the flap-wise root bending moment in response to changes in pitch angle, evaluated at the collective pitch angle $\bar{\theta}$, whilst $G_{\mathrm{a}}(s)$, $G_{\mathrm{b}}(s)$ and $G_{\mathrm{f}}(s)$ are, respectively, the transfer functions that describe the pitch actuator, blade, and sensor band-pass filter dynamics. These are defined as follows [10, 17]:

$$G_{\mathrm{a}}(s) := \frac{1}{\tau s + 1}, \tag{1b}$$

$$G_{\mathrm{b}}(s) := \left(\frac{\omega_{\mathrm{flap}}^2}{s^2 + 2\zeta_{\mathrm{b}}\omega_{\mathrm{flap}}s + \omega_{\mathrm{flap}}^2}\right)\left(\frac{\omega_{\mathrm{edge}}^2}{s^2 + 2\zeta_{\mathrm{b}}\omega_{\mathrm{edge}}s + \omega_{\mathrm{edge}}^2}\right), \tag{1c}$$

$$G_{\mathrm{f}}(s) := \frac{\omega_{\mathrm{h}}s}{s^2 + (\omega_{\mathrm{h}} + \omega_{\mathrm{l}})s + \omega_{\mathrm{h}}\omega_{\mathrm{l}}}. \tag{1d}$$

The parameters of these transfer functions are listed in Table I, with values representative of the NREL 5MW turbine [37], linearised around operation in above rated conditions. The actuator time constant is based upon a pitch actuator employed in a similarly rated commercial offshore turbine [10]. The band-pass filter (1d) is included in the system model to remove low-frequency drift and high frequency noise from the bending moment measurements, as well as reducing interaction with the CPC.

The aim of the IPC controller $K_{\mathrm{IPC}}(s) \in \mathcal{R}$ is to attenuate the effect of the lumped wind-induced disturbance torque $d_{\tilde{\tau}}$, particularly at the 1P frequency. The extent to which this is possible is dictated by the dynamics of the blade system. The bode plot of $G(s)$ is shown in Figure 2, where the 1P frequency ω_1 (1.27 rad/s) and natural frequency of the first flap-wise blade mode ω_{flap} (4.21 rad/s) are marked on the abscissa. Owing to the flap-wise modes, the open-loop phase is -180° at ω_{flap}, and decreases further with increasing frequency as subsequent poles from the edge-wise modes and actuator are encountered. In accordance with the Bode integral Theorem [38], there is thus a fundamental limitation on the achievable performance of the IPC controller. Even if a stabilising controller can be designed, the sensitivity to disturbances will become greatly amplified for any controller that sets the closed-loop bandwidth in excess of ω_{flap}. The requirement that the closed-loop bandwidth be in the vicinity of ω_{flap} is ensured by the loop transfer function $K_{\mathrm{IPC}}G(s)$ achieving unity gain crossover near this frequency. However, given the close proximity in frequency between ω_1 and ω_{flap}, it is difficult to simultaneously make $|KG(s)|$ large at the former (thereby achieving good 1P disturbance rejection), and small at the latter, particularly given that good robustness requires the slope of $|KG(s)|$ to not greatly exceed -20 dB/decade at crossover [38]. The situation is even more challenging for disturbance rejection at the higher 2P (2.53 rad/s) and 4P (5.07 rad/s) frequencies, which are known to contribute to the fatigue-inducing 3P loads of the non rotating turbine components [10]. Hence, the achievable performance of conventional IPC control is limited by the flap-wise blade dynamics, as opposed to the pitch actuator.

3. CASCADED IPC AND BLADE INFLOW MEASUREMENT

If the blade dynamics impose a performance limitation upon conventional IPCs, then what alternatives exist? From a pragmatic viewpoint, solutions should avoid costly hardware redesign, whilst employing simple controllers. The former suggests different/additional sensors, as opposed to new actuation schemes, and this perhaps explains the present research interest in LiDAR-based control. However, a simpler solution may exist in the form of a blade inflow sensor. Whilst not capable of providing a preview of an oncoming disturbance, blade inflow measurements at least provide information on the

Wind Energ. 2013; **00**:1–16 © 2013 John Wiley & Sons, Ltd.
DOI: 10.1002/we
Prepared using weauth.cls

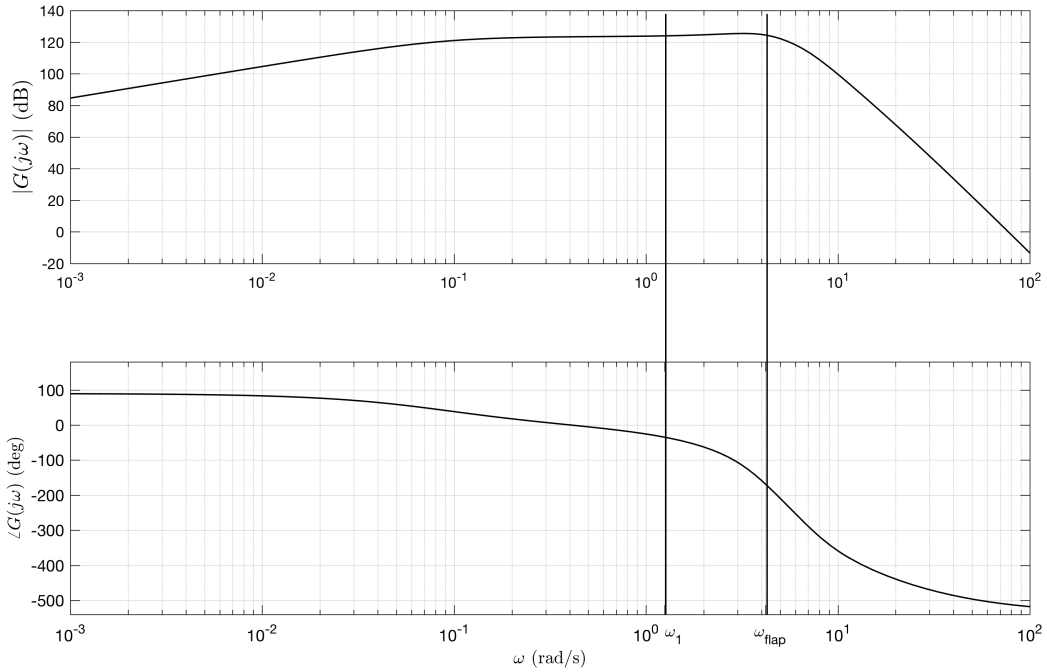

Figure 2. Bode plot of $G(s)$, with 1P frequency (ω_1) and natural frequency of the first flap-wise blade mode (ω_{flap}) indicated.

disturbance before it has propagated through the blades, thereby not experiencing the additional lag induced by the blade dynamics. Importantly, such measurements are suitable as the basis for designing new/additional feedback control loops, hence providing a mechanism to mitigate against the sensitivity to model uncertainty that is the achilles heel of feedforward methods. Motivated by this, we pose a novel IPC architecture that exploits feedback from blade inflow measurement on each blade.

3.1. Cascaded IPC architecture and analysis

Consider a blade discretised into n sections, each subjected to an aerodynamic lift force perturbation $\tilde{L}_i$ in the flap-wise direction and acting at a radial distance r_i from the blade root, where $i \in \{1, \ldots, n\}$. Then the parameter $(dM/d\theta)|_{\bar{\theta}}$ in (1a) can be expressed as follows:

$$\left.\frac{dM}{d\theta}\right|_{\bar{\theta}} = \sum_{i=1}^{n} \left.\frac{dL_i}{d\theta}\right|_{\bar{\theta}} r_i, \tag{2}$$

where $(dL_i/d\theta)|_{\bar{\theta}}$ is the sensitivity in the blade element lift force with respect to blade pitch angle, evaluated at the collective pitch angle. The corresponding change to the system diagram is shown in Figure 3. Dimensional analysis of the spanwise spatial extent of gusts suggests a similar spatial scale to the rotor radius of multi-MW turbines [34]. We therefore make the assumption that the disturbance lift forces $d_{\tilde{L}_k}$, acting on each blade element are spatially correlated, and at the very least, the disturbances acting on adjacent blade elements are of similar magnitude. A single sensor capable of measuring the aerodynamic lift force on a blade section (see Section 3.2) will therefore act as an approximate indicator of nearby loads. In terms of sensor placement, given that the highest blade loads occur near the tip [2] and are therefore the largest contributors to bending moment, we assume a (bandpass-filtered) measurement of aerodynamic lift force $y_{\tilde{L}_k}$ on the k-th blade element at a radial distance of $0.75R$ from the hub. Similar reasoning is applied in other control studies using local inflow measurements [26], or where the lift forces are lumped to a single point load [8].

Crucially, such a measurement enables the design of a cascaded feedback controller K_{C}, as shown in Figure 3, in which the cascaded loop does not contain the blade dynamics G_{b}. Cascade control ([39] and references therein) extends the benefits of feedback control to localised subsystems. In the present application, the cascaded controller provides a second degree-of-freedom in terms of rejecting the effect of the aerodynamic disturbances. To see this more clearly consider the dynamics of the cascaded loop in Figure 3:

$$\tilde{\tau}_k(s) = \frac{r_k \left.\frac{dL_k}{d\theta}\right|_{\bar{\theta}} G_{\text{a}}(s)}{1 - \left.\frac{dL_k}{d\theta}\right|_{\bar{\theta}} G_{\text{a}}(s)K_{\text{C}}(s)G_{\text{f}}(s)} u_{\text{IPC}}(s) + \frac{r_k}{1 - \left.\frac{dL_k}{d\theta}\right|_{\bar{\theta}} G_{\text{a}}(s)K_{\text{C}}(s)G_{\text{f}}(s)} d_{\tilde{L}_k}(s). \tag{3}$$

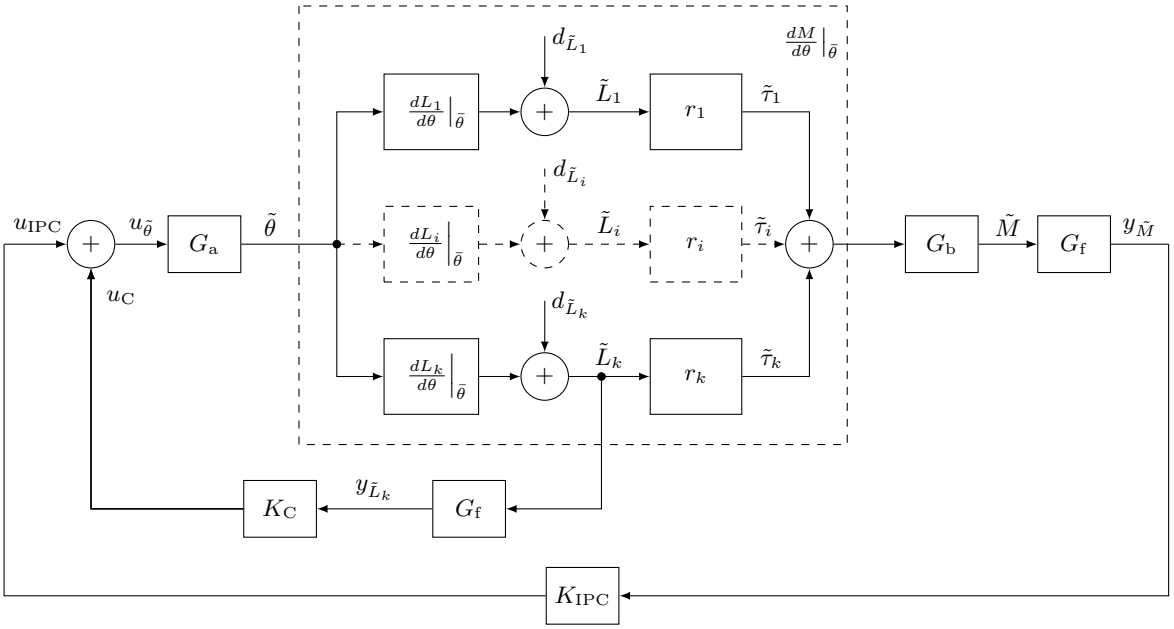

Figure 3. Single blade cascaded IPC system diagram, assuming a blade inflow measurement on the k-th blade element. This is the same system as shown in Figure 1, with the exception of the additional cascaded feedback loop.

Hence, the effect of the measured aerodynamic disturbance can be attenuated by making K_{C} large. Since the blade dynamics (G_{b}) are not present in (3), the bandwidth limitation associated with this term is removed, making it easier to achieve the higher loop gains commensurate with improved performance. Indeed, the limitation now arises from the actuator dynamics, with the maximum pitch rate likely to be the limiting factor. To see the effect the cascaded controller has upon the remaining blade sections, consider the dynamics of the i-th loop in Figure 3:

$$\tilde{\tau}_i(s) = r_i \left(d_{\tilde{L}_i}(s) + \frac{dL_i}{d\theta}\bigg|_{\bar{\theta}} G_{\mathrm{a}}(s)(u_{\mathrm{IPC}}(s) + u_{\mathrm{C}}(s)) \right), \tag{4a}$$

where:

$$u_{\mathrm{C}}(s) = \frac{K_{\mathrm{C}}(s)G_{\mathrm{f}}(s)}{1 - K_{\mathrm{C}}(s)G_{\mathrm{f}}(s)\ \frac{dL_k}{d\theta}\big|_{\bar{\theta}} G_{\mathrm{a}}(s)} d_{\tilde{L}_k}(s) + \frac{K_{\mathrm{C}}(s)G_{\mathrm{f}}(s)\ \frac{dL_k}{d\theta}\big|_{\bar{\theta}} G_{\mathrm{a}}(s)}{1 - K_{\mathrm{C}}(s)G_{\mathrm{f}}(s)\ \frac{dL_k}{d\theta}\big|_{\bar{\theta}} G_{\mathrm{a}}(s)} u_{\mathrm{IPC}}(s). \tag{4b}$$

Substituting (4b) into (4a) yields:

$$\tilde{\tau}_i(s) = r_i \left(d_{\tilde{L}_i}(s) + \frac{\frac{dL_i}{d\theta}\big|_{\bar{\theta}} G_{\mathrm{a}}(s)K_{\mathrm{C}}(s)G_{\mathrm{f}}(s)}{1 - K_{\mathrm{C}}(s)G_{\mathrm{f}}(s)\ \frac{dL_k}{d\theta}\big|_{\bar{\theta}} G_{\mathrm{a}}(s)} d_{\tilde{L}_k}(s) + \frac{\frac{dL_i}{d\theta}\big|_{\bar{\theta}} G_{\mathrm{a}}(s)}{1 - K_{\mathrm{C}}(s)G_{\mathrm{f}}(s)\ \frac{dL_k}{d\theta}\big|_{\bar{\theta}} G_{\mathrm{a}}(s)} u_{\mathrm{IPC}}(s) \right). \tag{4c}$$

For the frequencies at which K_{C} is large, the third term in (4c) is negligible, and provided $dL_i/d\theta \approx dL_k/d\theta$ and $d_{\tilde{L}_i} \approx d_{\tilde{L}_k}$, as assumed for blade elements adjacent to the k-th element where the sensor is located, then the first two terms will approximately cancel. The degree of cancellation will likely degrade for blade elements nearest the root, but this is of little concern given the relatively small contribution that such elements make to the overall blade-root bending moment.

The equivalent block diagram is shown in Figure 4, where the cascaded controller not only modifies the gain $(dM/d\theta)|_{\bar{\theta}}$, but also influences the loading from each blade element in response to the individual disturbance lift forces. Note, this cascaded IPC system reduces to the conventional IPC case (Figure 1) when $K_{\mathrm{C}} = 0$, as is to be expected. The sensitivity function $S_{d_{\tilde{L}_k} \to y_{\tilde{M}}}$ from measured disturbance $d_{\tilde{L}_k}$ to measured flap-wise blade-root bending moment $y_{\tilde{M}}$ is given by:

$$S_{d_{\tilde{L}_k} \to y_{\tilde{M}}} = \frac{r_k G_{\mathrm{b}}(s)G_{\mathrm{f}}(s)}{1 - \frac{dL_k}{d\theta}\big|_{\bar{\theta}} G_{\mathrm{a}}(s)K_{\mathrm{C}}(s)G_{\mathrm{f}}(s) - \frac{dM}{d\theta}\big|_{\bar{\theta}} G_{\mathrm{a}}(s)G_{\mathrm{b}}(s)G_{\mathrm{f}}(s)K_{\mathrm{IPC}}(s)}. \tag{5}$$

This sensitivity function is made small by making K_{C} and/or K_{IPC} large at the frequencies of interest. Given the advantages of using the cascaded controller to achieve higher loop gain, it would seem that K_{IPC} is rendered obsolete.

DOI: 10.1002/we
Prepared using weauth.cls

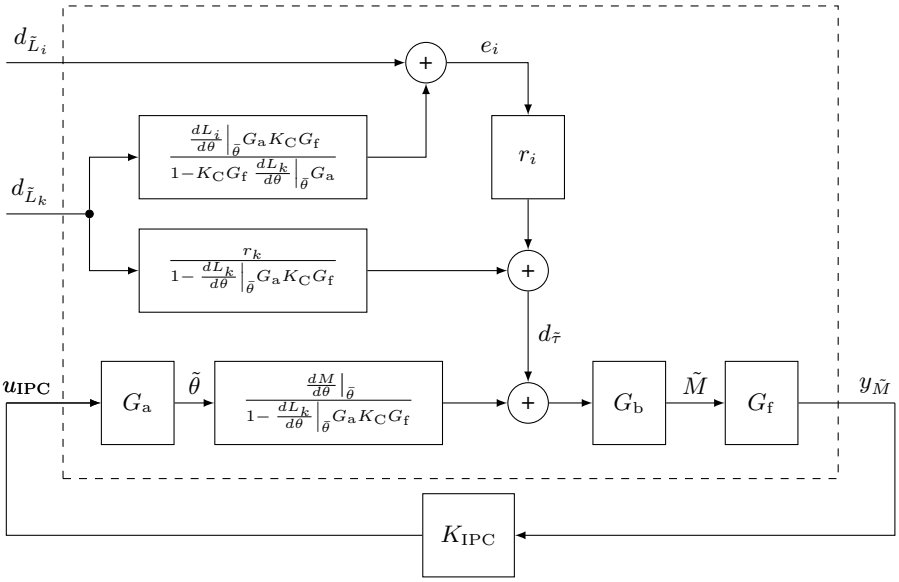

Figure 4. Equivalent cascaded IPC system diagram, showing the contribution of the blade section lift disturbances $d_{\tilde{L}_i}$ to the wind induced flap-wise disturbance torque $d_{\tilde{\tau}}$ under the action of K_C.

However, this is not the case. Recall from (4c) that attenuating the effect of the unmeasured blade disturbances $d_{\tilde{L}_i}$ relies upon the following error terms being made small:

$$e_i(s) := d_{\tilde{L}_i}(s) + \frac{\frac{dL_i}{d\theta}\Big|_{\bar{\theta}} G_\mathrm{a}(s)K_\mathrm{C}(s)G_\mathrm{f}(s)}{1 - K_\mathrm{C}(s)G_\mathrm{f}(s)\ \frac{dL_k}{d\theta}\Big|_{\bar{\theta}} G_\mathrm{a}(s)} d_{\tilde{L}_k}(s). \tag{6}$$

This is essentially a feedforward control strategy that relies upon the assumptions outlined beneath (4c). It is possible that unusual inflow conditions of localised wind-shear may arise that could make this error large, resulting in undesirable blade loads. However, the additional feedback action from K_IPC acts to suppress such loads as can be seen by inspecting the sensitivity function $S_{e_i \to y_{\tilde{M}}}$ from disturbance error to measured flap-wise blade-root bending moment:

$$S_{e_i \to y_{\tilde{M}}} = \frac{G_\mathrm{f}(s)G_\mathrm{b}(s)r_i\left(1 - K_\mathrm{C}(s)G_\mathrm{f}(s)\ \frac{dL_k}{d\theta}\Big|_{\bar{\theta}} G_\mathrm{a}(s)\right)}{1 - \frac{dL_k}{d\theta}\Big|_{\bar{\theta}} G_\mathrm{a}(s)K_\mathrm{C}(s)G_\mathrm{f}(s) - \frac{dM}{d\theta}\Big|_{\bar{\theta}} G_\mathrm{a}(s)G_\mathrm{b}(s)G_\mathrm{f}(s)K_\mathrm{IPC}(s)}. \tag{7}$$

Note that increasing K_IPC reduces this sensitivity towards zero, whereas increasing K_C results in the sensitivity approaching a nonzero constant. To summarise, the majority of the disturbance rejection is handled by the cascaded controller, with the IPC controller providing a degree of mitigation against excessive blade loading that may arise from unusual flow conditions not being detected by a single inflow sensor.

3.2. Determining blade element lift from local inflow measurement

The preceding analysis assumed a measurement of the aerodynamic lift force on a blade section. To our knowledge, no previous study on the use of local inflow measurements has used this specific signal as the basis for subsequent control, tending to use angle-of-attack and/or relative velocity information instead (e.g [26, 27]). To see how the lift force can be determined in practice consider a pitot-static tube mounted on the leading edge of an airfoil section (Figure 5) that provides direct measurements of the inflow angle of attack $\alpha(t) \in \mathbb{R}$ and relative windspeed $v_\mathrm{rel}(t) \in \mathbb{R}$. A momentary increase in the free-stream velocity $v_\infty(t) \in \mathbb{R}$ causes an increase in the angle of attack and relative windspeed. The resulting lift force (relative to the direction of $v_\mathrm{rel}(t)$) is given by [2]:

$$L_{\mathrm{rel},k}(t) = \frac{1}{2}\rho v_\mathrm{rel}^2(t) C_l(\alpha) c \delta_r, \tag{8a}$$

where $\rho, c, \delta_r \in \mathbb{R}$ denote the density of air, blade chord length and span-wise section length, respectively. The blade section lift coefficient is given by [2]:

$$C_l(\alpha) = \frac{dC_l}{d\alpha}\sin(\alpha(t)) \approx \frac{dC_l}{d\alpha}\alpha, \tag{8b}$$

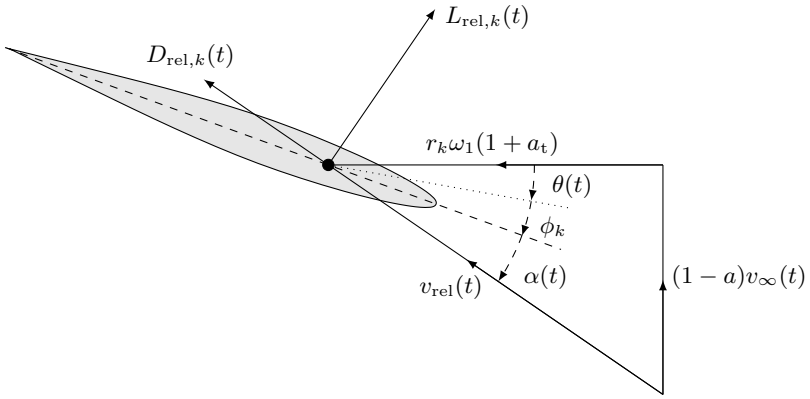

Figure 5. Blade element velocities and forces, where a and a_t are the axial and tangential flow induction factors, respectively [2].

where $dC_l/d\alpha \in \mathbb{R}$ is the airfoil section lift-curve slope (e.g. [37]) and where the approximation is valid for small angles of attack in the pre-stall region. Similarly, the relative drag is:

$$D_{\mathrm{rel},k}(t) = \frac{1}{2}\rho v_{\mathrm{rel}}^2(t) C_d c \delta_r, \tag{8c}$$

where $C_d \in \mathbb{R}$ is the drag coefficient, which for blades of large span is ~ 0.01 [2]. Assuming the flap-wise direction is defined normal to the blade zero-twist reference, then the aerodynamic load in the flap-wise direction is as follows:

$$L_k(t) = L_{\mathrm{rel},k}(t)\cos(\phi_k) + D_{\mathrm{rel},k}(t)\sin(\phi_k), \tag{9}$$

where $\phi_k \in \mathbb{R}$ is the blade section twist angle. In summary, measurements of angle of attack and relative windspeed, combined with several known aerodynamic parameters, enables the lift force acting on an airfoil section to be determined.

4. CONTROLLER DESIGN AND SIMULATION RESULTS

This section demonstrates the performance benefits of cascaded IPC over conventional IPC, with the respective architectures shown in Figures 3 and 1. Specifically, the primary objective of both controllers is to maximise the attenuation of 1P disturbances for a fixed robust stability margin $\epsilon(G,K)$ [40, 10, 17]:

$$\epsilon(G,K) := \begin{cases} \Big\| \underbrace{\begin{bmatrix} G \\ I \end{bmatrix} (I-KG)^{-1} \begin{bmatrix} -K & I \end{bmatrix}}_{H(G,K)} \Big\|_\infty^{-1} & \text{if } H(G,K) \in \mathcal{RH}_\infty \\ 0 & \text{otherwise,} \end{cases} \tag{10}$$

where $\mathcal{RH}_\infty$ is the space of proper real-rational transfer function matrices of stable, linear and time-invariant continuous-time systems with norm $\|\cdot\|_\infty$. The robust stability margin is a generalisation of gain and phase margin, and so acts as a convenient scalar measure of robust stability and performance. In the interests of fair comparison, the robust stability margin of both controllers is set to the same value $\epsilon(G,K) = 0.40$.

4.1. Conventional IPC design

The conventional IPC controller takes the form of a proportional gain in series with a 1P inverse notch filter:

$$K_{\mathrm{IPC}}(s) := -k_\mathrm{p}\left(\frac{s^2 + 2\zeta_1\omega_1 s + \omega_1^2}{s^2 + 2\zeta_2\omega_1 s + \omega_1^2}\right), \tag{11}$$

where the parameters are listed in Table II. The Bode plots of the shaped loop $GK_{\mathrm{IPC}}(j\omega)$ are shown in Figure 6, with the sensitivity function (5) shown in Figure 9. More complex compensators that improve the 1P disturbance rejection for the same stability margin are of course possible, but for the purposes of this study are not considered.

DOI: 10.1002/we
Prepared using weauth.cls

Parameter	Value	Units	Description
k_p	2.05×10^{-7}	deg/Nm	Proportional gain
ζ_1	0.5		First inverse notch filter damping ratio
ζ_2	0.01		Second inverse notch filter damping ratio
ω_1	1.27	rad/s	1P frequency

Table II. Parameters of $K_\mathrm{IPC}(s)$ (11).

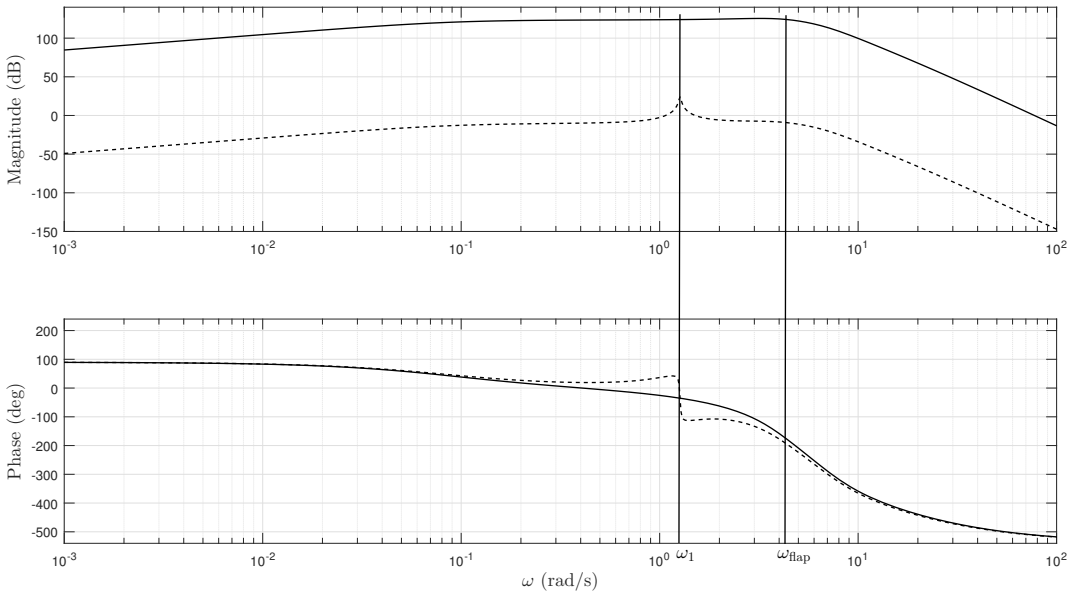

Figure 6. Magnitude and phase plots of the shaped GK_IPC (- -) and unshaped G (–) blade systems, using conventional IPC.

Parameter	Value	Units	Description
k_p	5.00×10^{-4}	deg/Nm	Proportional gain
ζ_1	1		First inverse notch filter damping ratio
ζ_2	0.1		Second inverse notch filter damping ratio
ω_1	1.27	rad/s	1P frequency

Table III. Parameters of $K_\mathrm{C}(s)$.

4.2. Cascaded IPC design

The cascaded IPC design proceeds with the design of the inner loop. Referring to Figure 3, the transfer function of the unshaped inner loop is as follows:

$$G_\mathrm{inner}(s) := \left.\frac{dL_k}{d\theta}\right|_{\bar{\theta}} G_\mathrm{a}(s)G_\mathrm{f}(s). \tag{12}$$

The cascaded controller K_C again takes the form of an inverted notch filter, centred upon the 1P frequency (11), but the more benign dynamics of the inner loop allow for a broader notch, thus extending disturbance rejection to 2P and 4P frequencies. The proportional gain k_p is chosen to provide an upper unity gain crossover at around the same frequency as the actuator pole, in order to prevent excessive actuator usage. The parameters of K_C are listed in Table III, and the bode plots of the shaped and unshaped inner loops shown in Figure 7. The robust stability margin of the compensated inner loop was $\epsilon(G_\mathrm{inner}, K_\mathrm{C}) = 0.56$, exceeding the stated margin of 0.40.

Proceeding to the outer loop, with reference to Figure 4 the design of K_IPC is based upon shaping the outer-loop transfer function:

$$G_\mathrm{outer}(s) := \frac{\left.\frac{dM}{d\theta}\right|_{\bar{\theta}} G_\mathrm{a}(s)G_\mathrm{b}(s)G_\mathrm{f}(s)}{1 - \left.\frac{dL_k}{d\theta}\right|_{\bar{\theta}} G_\mathrm{a}(s)K_\mathrm{C}(s)G_\mathrm{f}(s)}. \tag{13}$$

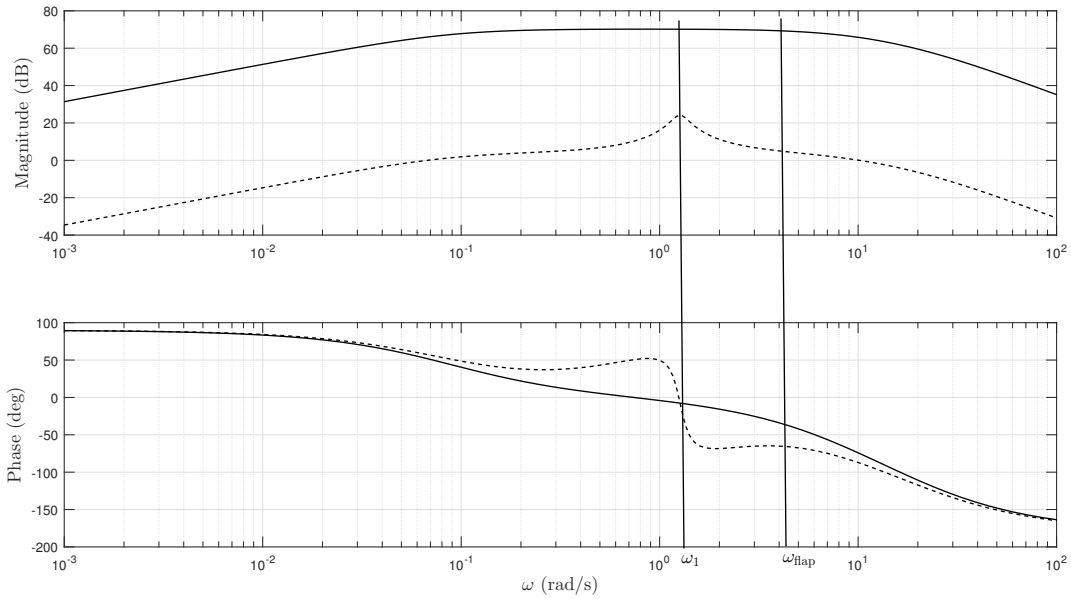

Figure 7. Magnitude and phase plots of the shaped $G_{\text{inner}}K_{\text{C}}$ (- -) and unshaped G_{inner} (–) inner loop.

Parameter	Value	Units	Description
k_{p}	5.95×10^{-7}	deg/Nm	Proportional gain
ζ_1	0.5		First inverse notch filter damping ratio
ζ_2	0.01		Second inverse notch filter damping ratio
ω_1	1.27	rad/s	1P frequency

Table IV. Parameters of the IPC controller $K_{\text{IPC}}(s)$ used in the cascaded design.

The outer IPC controller K_{IPC} again takes the form of an inverted notch filter, centred upon the 1P frequency (11). The parameters of this controller are listed in table IV and are chosen to provide additional 1P disturbance rejection, whilst ensuring $\epsilon(G_{\text{outer}}, K_{\text{IPC}}) = 0.40$.

The bode plots of $G_{\text{outer}}(j\omega)$ and $G_{\text{outer}}K_{\text{IPC}}(j\omega)$ are shown in Figure 8, with the sensitivity function (5) shown in Figure 9. The sensitivity plots of Figure 9 clearly display the improved performance of the cascaded architecture. For the same robust stability margin, the cascaded design achieves an additional ~ 10 dB disturbance rejection at the 1P frequency, in addition to greater disturbance rejection at nearby frequencies, including 2P and 4P.

4.3. Simulation Results

This section investigates the performance of the proposed IPC controllers for attenuating the fatigue and extreme loads on the turbine blades. Three controllers were considered in this study as follows:

1. the CPC (Baseline),
2. the conventional IPC in Section 4.1 (K_{IPC}),
3. the cascaded IPC in Section 4.2 ($K_{\text{IPC}} + K_{\text{C}}$).

The simulation environment employed for this purpose is FAST [41] and the closed-loop simulations were conducted upon the NREL 5MW turbine [37], with key parameters listed in Table V. This turbine model is of much greater complexity than the model employed in (1) for controller design. The additional degrees-of-freedom include the first and second modes of the blade flap-wise and edge-wise modes, in addition to the tower and shaft dynamics. The baseline CPC controller is unchanged from that described in [37].

4.3.1. Fatigue load reductions

The controller performance with respect to fatigue load reductions was investigated under turbulent wind conditions generated from TurbSim [42]. The full, three dimensional wind-field was characterised by a mean wind speed of 18 ms^{-1} (chosen since this value is near the centre of the range of wind speeds covering above-rated wind conditions), a turbulence

Wind Energ. 2013; **00**:1–16 © 2013 John Wiley & Sons, Ltd.
DOI: 10.1002/we
Prepared using weauth.cls

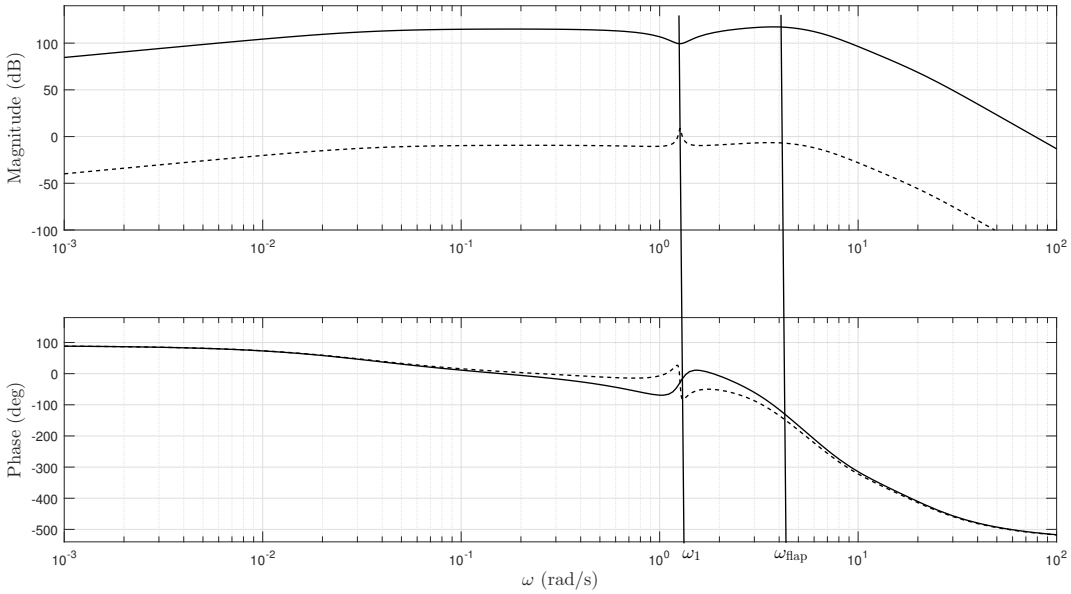

Figure 8. Magnitude and phase plots of the shaped $G_{\text{outer}}K_{\text{IPC}}$ (- -) and unshaped G_{outer} (–) outer loops of the cascaded system.

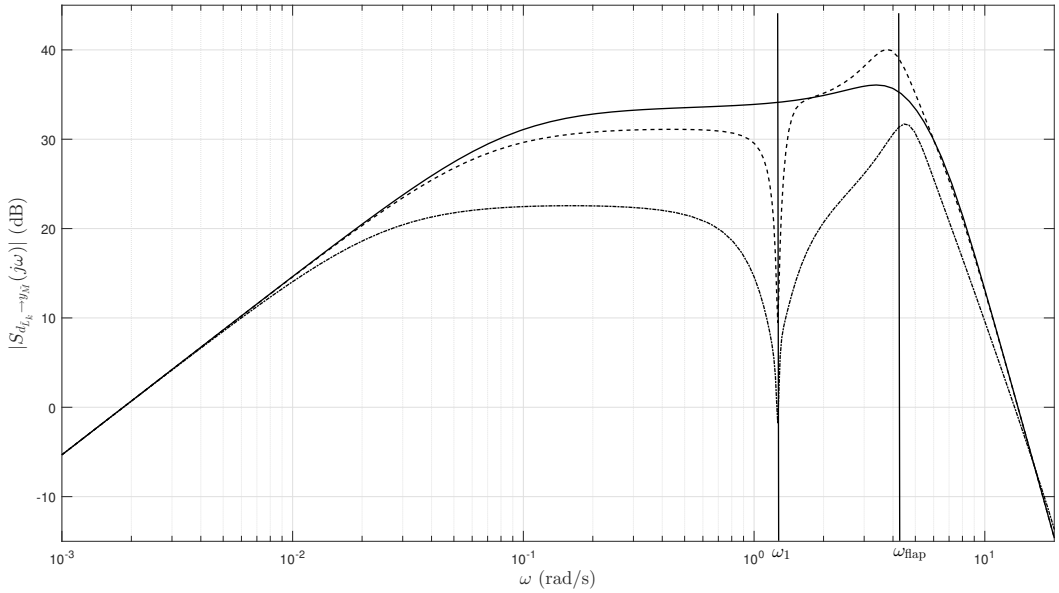

Figure 9. Sensitivity (5) plots of the uncompensated blade system (–), the blade system controlled with conventional IPC ($K_{\text{C}} = 0$, K_{IPC} (Table II)) (- -), and the blade system controlled with cascaded IPC (K_{C} (Table III), K_{IPC} (Table IV)) (-·). Note the significantly lower sensitivity achieved by the cascaded controller.

Parameter	Value
Rating	5 MW
Rotor Orientation	Upwind
Rotor diameter	126 m
Hub height	90 m
Rated rotor speed	12.1 rpm ($\approx$ 1.27 rad/s)
Pitch rate limit	$\pm 8^\circ/\text{s}$

Table V. Turbine simulation parameters.

intensity of 14% and a vertical shear power law exponent of 0.2. The simulations were performed for sufficient duration to obtain convergence in the blade load spectra.

Figures 10a and 10b show the time history and load spectrum of the flap-wise blade root bending moment for each controller. The conventional and cascaded IPC controllers both performed better in terms of reducing the blade loads compared to the baseline CPC case. However, the cascaded IPC architecture achieved a significant further 60% reduction in 1P blade loads, compared to the conventional IPC controller. In terms of the blade pitch activity, shown in Figures 10c and 10d, the cascaded IPC architecture used slightly more actuation effort than the conventional IPC, with the standard deviations of pitch angle and pitch rate being 9% and 16% greater, respectively. This is to be expected given the shaping of the inner-loop of the cascaded controller, where the bandwidth of the inner loop was not limited by the blade first flap-wise mode. A conventional IPC controller would of course also demonstrate superior performance if the pitch actuator was allowed to work harder, but only at the expense of reducing the controller's robust stability margin. For the same stability margin, the cascaded controller demonstrates a greater ability to utilise the available performance of the pitch actuator, owing to the more benign dynamics of the inner loop (12), where the limiting flapwise-modes are not present. The numerical results from the full 20-minute simulation are summarised in Table VI.

	CPC (Baseline)	Conventional IPC	Cascaded IPC
$\lvert M_1(\omega)\rvert$ at 1p frequency [kNm]	1218 (100%)	107.8 (9%)	42.3 (3%)
$\mathrm{std}(\theta_1(t))$ [deg]	1.35 (100%)	1.80 (133%)	1.93 (142%)
$\mathrm{std}(\dot{\theta}_1(t))$ [degs^{-1}]	2.30 (100%)	2.80 (122%)	3.17 (138%)
Blade root M DEL [kNm]	1381 (100%)	766 (55%)	682 (49%)

Table VI. Numerical results obtained from the full 20-minute simulations under a turbulent wind field. The notation $|\cdot|$ denotes amplitude, whilst std is the standard deviation. Damage equivalent loads (DELs) were computed using the Palmgren-Miner rule and rain-flow counting algorithm [43, 44], with the material-specific parameter of 10.

4.3.2. Extreme load reductions

Since IPC is particularly designed to attenuate asymmetrical loads on the rotor, an extreme wind shear case was chosen to demonstrate the performance of the cascaded architecture on an extreme load case of relevance. An extreme wind shear profile was modelled as follows [2]:

$$v(z,t) := v_{\mathrm{hub}}(t)\left(\frac{z}{z_{\mathrm{hub}}}\right)^{0.2} + v_{\mathrm{shear}}(z,t), \tag{14a}$$

where $z \in \mathbb{R}$ is the vertical distance from the tower base, $z_{\mathrm{hub}} = 90$ m is the hub height and $v_{\mathrm{hub}} = 18$ ms^{-1} is the wind speed at this height. The additional vertical transient wind shear $v_{\mathrm{shear}} \in \mathbb{R}$ is defined as:

$$v_{\mathrm{shear}}(z,t) := \left(\frac{z - z_{\mathrm{hub}}}{D}\right)\left(2.5 + 0.2\beta\sigma_u\left(\frac{D}{\Lambda}\right)^{0.25}\right)\left(1 - \cos\left(\frac{2\pi t}{T}\right)\right), \tag{14b}$$

where $D = 2R$ is the diameter of the rotor, $\beta,\ \sigma_u,\ \Lambda \in \mathbb{R}$ are the turbulence scale parameters [2] and $T = 12$ s is the duration of the transient wind shear. Figure 11 shows the correspondingtemporal change in wind speed across the rotor plane in the vertical section created by (14).

Under the transient extreme wind shear, Figure 12a shows the time history of the blade flap-wise root bending moment. The cascaded IPC again achieved significant blade load attenuation, compared to the baseline CPC and conventional IPC designs. Whereas the conventional IPC controller only yielded a 16% attenuation in blade loads, the cascaded design achieved a much greater reduction. Compared to the conventional IPC, the cascaded controller yielded a blade load reduction of 59%. Again, this is to be expected owing to the cascaded IPC's ability to fully utilise the pitch actuator without compromising the robust stability margin, arising from the fact that the cascaded controller can react more quickly in response to a measurement with less lag. The pitch activities in Figure 12b and 12c shows the cascaded IPC responding to wind speed changes much faster than the conventional IPC. The numerical results are summarised in Table VII.

5. CONCLUSIONS

This paper was concerned with significantly improving IPC performance in a simple and pragmatic fashion. The limitations of conventional IPC controllers arise from the phase-lag associated with the blade dynamics, making it difficult to fully exploit the available pitch actuation without compromising the stability of the system. Motivated by this, a simple solution

Wind Energ. 2013; **00**:1–16 © 2013 John Wiley & Sons, Ltd.
DOI: 10.1002/we
Prepared using weauth.cls

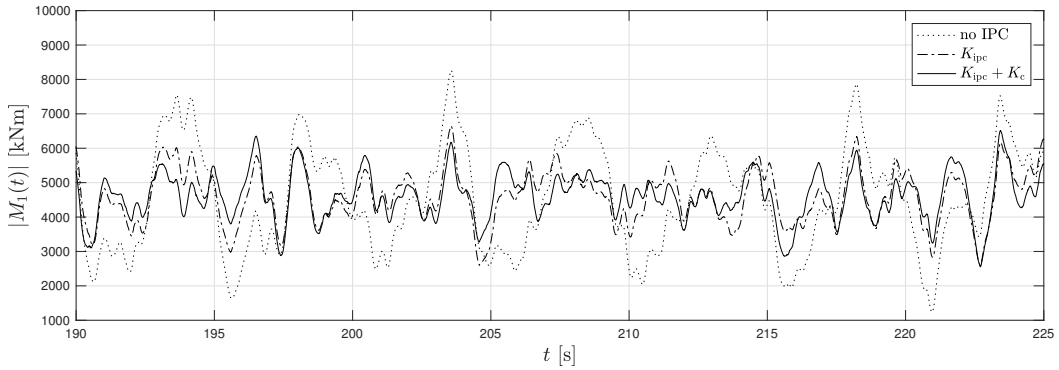

(a) Time history of the blade flap-wise root bending moment of blade 1.

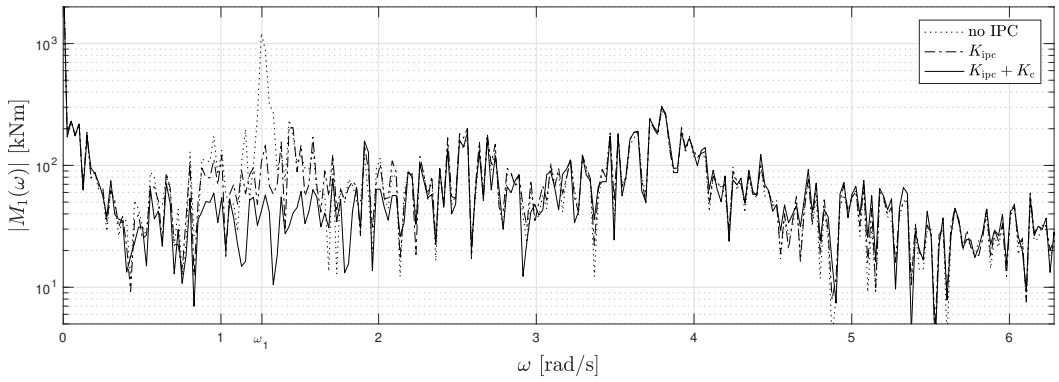

(b) Load spectrum of the blade flap-wise root bending moment of blade 1. Note the significant additional load reductions achieved by the cascaded IPC around the 1P frequency.

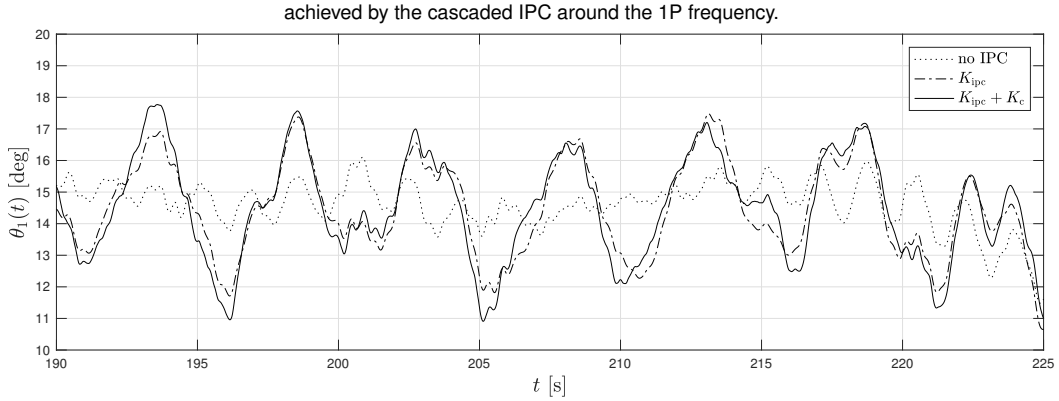

(c) Time history of the pitch angle of blade 1.

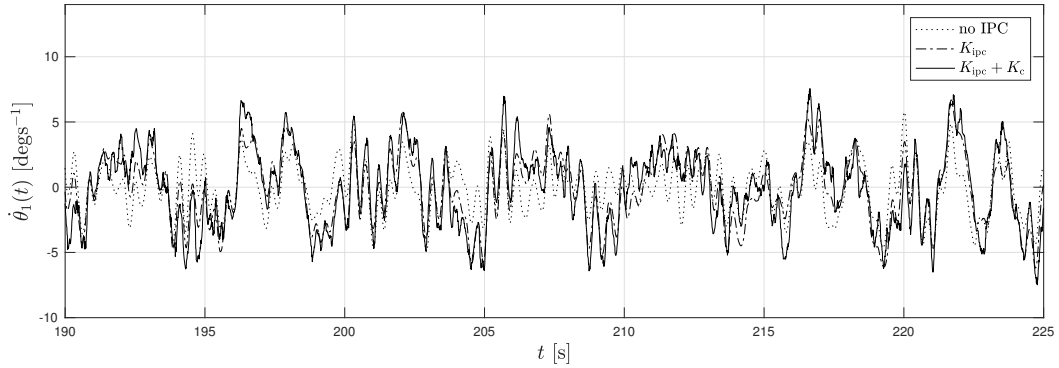

(d) Time history of the pitch rate of blade 1.

Figure 10. Simulation results upon the NREL 5MW turbine under a turbulent wind field, showing the performance of the baseline CPC (dotted line), conventional IPC (dash-dot line) and cascaded IPC (solid line). Similar results were obtained for the remaining blades.

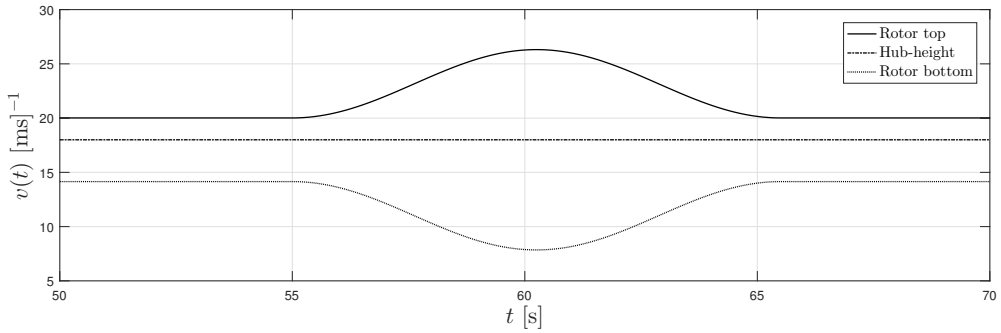

Figure 11. The extreme wind shear event employed in this work. Wind speeds are plotted at the rotor top (solid line), hub-height (dash-dot line) and rotor bottom (dotted line).

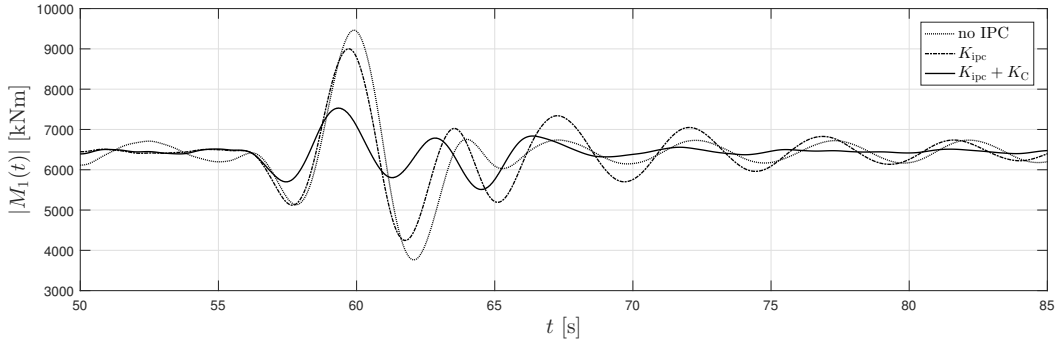

(a) Time history of the blade flap-wise root bending moment of blade 1.

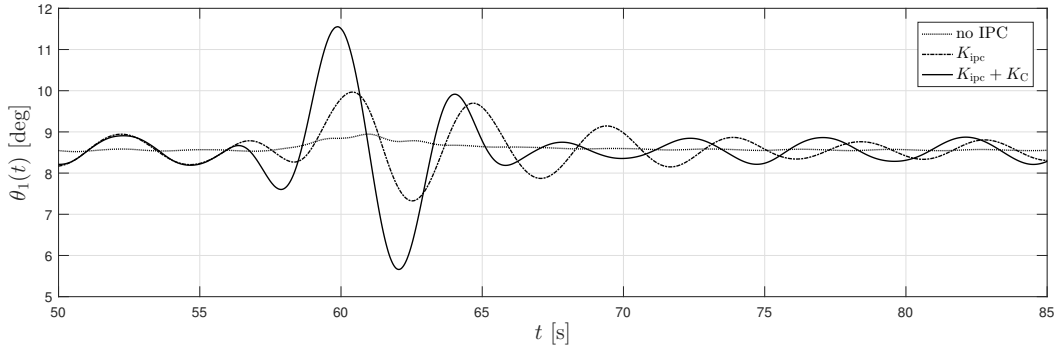

(b) Time history of the pitch angle of blade 1.

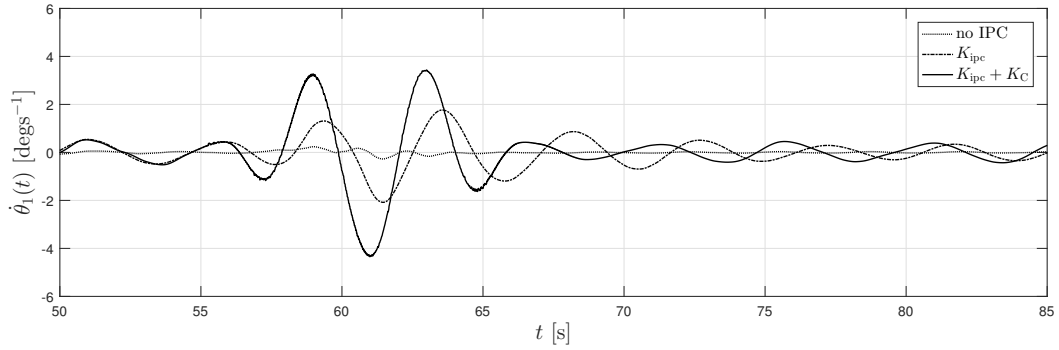

(c) Time history of the pitch rate of blade 1.

Figure 12. Simulation results upon the NREL 5MW turbine under extreme wind shear, showing the performance of the baseline CPC (dotted line), conventional IPC (dash-dot line) and cascaded IPC (solid line). Similar results were obtained for the remaining blades.

Wind Energ. 2013; **00**:1–16 © 2013 John Wiley & Sons, Ltd.
DOI: 10.1002/we
Prepared using weauth.cls

	CPC (Baseline)	Conventional IPC	Cascaded IPC
$\max(\lvert\tilde{M}_1(t)\rvert)$ [kNm]	2964 (100%)	2501(84%)	1032 (35%)
$\max(\lvert\tilde{\theta}_1(t)\rvert)$ [deg]	0.39 (100%)	1.41(362%)	3.00 (769%)
$\max(\lvert\dot{\tilde{\theta}}_1(t)\rvert)$ [degs^{-1}]	0.24 (100%)	1.76 (733%)	3.43 (1429%)

Table VII. Numerical results obtained from the simulations under the extreme wind shear. Mean values were $\bar{M} = 6500\,\mathrm{kNm}$, $\bar{\theta} = 8.55^\circ$, and $\bar{\dot{\theta}} = 0^\circ/\mathrm{s}$.

was proposed to bypass the blade dynamics, based upon an inflow sensor on each blade providing 'faster' information on the local aerodynamic lift force. This measurement enabled the design of an additional cascaded feedback loop that did not suffer from the limitations imposed by the blade dynamics. As a result, significant performance benefits were achieved, compared to a conventional IPC controller with the same robust stability margin. Simulation results showed the cascaded IPC controller achieving a 60% reduction in 1P blade fatigue loads, and a 59% reduction in extreme wind-shear induced blade loads. It is not clear if an alternative approach to mitigating IPC results using LiDAR would offer superior performance benefits. However, one important benefit of the cascaded IPC approach over LiDAR is its simplicity. This arises from the fact that it employs feedback, rather than feedforward control, hence reducing the sensitivity to model uncertainty. In particular, the use of an inflow sensor eliminates the need for employing accurate models relating upwind line-of-sight velocity measurements to future blade loads.

Future work may explore the necessary fault-tolerant control aspects of employing pitot-tubes as inflow sensors. The cascaded IPC might also be designed for below-rated conditions and also extended to the CPC loop for improved mitigation of extreme gust-induced loads.

REFERENCES

1. Bossanyi EA. Wind Turbine Control for Load Reduction. *Wind Energy* 2003; **6**(3):229–244.
2. Burton T, Jenkins N, Sharpe D, Bossanyi E. *Wind energy handbook*. Wiley, 2011.
3. Solingen E, Wingerden J. Linear individual pitch control design for two-bladed wind turbines. *Wind Energy* 2015; **18**(4):677–697.
4. Bossanyi E. Individual Blade Pitch Control for Load Reduction. *Wind Energy* 2003; **6**(2):119–128.
5. van Engelen TG. Design model and load reduction assessment for multi-rotational mode individual pitch control (higher harmonics control). *European Wind Energy Conference*, March, 2006; 6–68.
6. Bossanyi EA. Further load reductions with individual pitch control. *Wind Energy* 2005; **8**(4):481–485.
7. Stol K, Moll H, Bir G, Namik H. A comparison of multi-blade coordinate transformation and direct periodic techniques for wind turbine control design. *47th AIAA/ASME*, January, 2009; 1–12.
8. Selvam K, Kanev S, van Wingerden JW, van Engelen T, Verhaegen M. Feedback–feedforward individual pitch control for wind turbine load reduction. *International Journal of Robust and Nonlinear Control* 2009; **19**(1):72–91.
9. Navalkar S, Van Wingerden J, Van Solingen E, Oomen T, Pasterkamp E, Van Kuik G. Subspace predictive repetitive control to mitigate periodic loads on large scale wind turbines. *Mechatronics* 2014; **24**(8):916–925.
10. Lu Q, Bowyer R, Jones B. Analysis and design of Coleman transform-based individual pitch controllers for wind-turbine load reduction. *Wind Energy* 2015; **18**(8):1451–1468.
11. Bossanyi E, Wright A. Field testing of individual pitch control on the NREL CART-2 wind turbine. *EWEC2009-European Wind Energy Conference & Exhibition*, 2009.
12. Geyler M, Caselitz P. Robust multivariable pitch control design for load reduction on large wind turbines. *Journal of solar energy engineering* 2008; **130**(3):030 301–1.
13. Lackner MA, van Kuik G. A comparison of smart rotor control approaches using trailing edge flaps and individual pitch control. *Wind Energy* 2010; **13**(2-3):117–134.
14. Plumley C, Leithead W, Jamieson P, Bossanyi E, Graham M. Comparison of individual pitch and smart rotor control strategies for load reduction. *The Science of Making Torque from Wind 2014 (TORQUE 2014)* 2014; **524**:012 054.
15. Leithead WE, Neilson V, Dominguez S, Dutka A. A novel approach to structural load control using intelligent actuators. *Mediterranean Conference on Control & Automation*, 2009; 1257–1262.
16. Leithead W, Neilson V, Dominguez S. Alleviation of unbalanced rotor loads by single blade controllers. *European Wind Energy Conference*, 2009.
17. Lio WH, Jones BL, Lu Q, Rossiter J. Fundamental performance similarities between individual pitch control strategies for wind turbines. *International Journal of Control* 2017; **90**(1):37–52.

18. Scott S, Capuzzi M, Langston D, Bossanyi E, McCann G, Weaver P, Pirrera A. Gust response of aeroelastically tailored wind turbines. *Journal of Physics: Conference Series*, vol. 753, IOP Publishing, 2016; 042 006.
19. Lobitz DW, Veers PS. Load mitigation with bending/twist-coupled blades on rotors using modern control strategies. *Wind Energy* 2003; **6**(2):105–117.
20. Barlas T, van Kuik G. Review of state of the art in smart rotor control research for wind turbines. *Progress in Aerospace Sciences* 2010; **46**(1):1–27.
21. Ng BF, Palacios R, Kerrigan EC, Graham JMR, Hesse H. Aerodynamic load control in horizontal axis wind turbines with combined aeroelastic tailoring and trailing-edge flaps. *Wind Energy* 2016; **19**(2):243–263.
22. Johnson SJ, Baker JP, Van Dam C, Berg D. An overview of active load control techniques for wind turbines with an emphasis on microtabs. *Wind Energy* 2010; **13**(2-3):239–253.
23. Nelson RC, Corke TC, Othman H, Patel MP, Vasudevan S, Ng T. A smart wind turbine blade using distributed plasma actuators for improved performance. *Proceedings of the 46th Aerospace Sciences Meeting, Reno, NV, Jan*, 2008; 7–10.
24. Maldonado V, Farnsworth J, Gressick W, Amitay M. Active enhancement of wind turbine blades performance. *46th AIAA Aerospace Sciences Meeting and Exhibit*, 2008; 1311.
25. Cooperman A, Martinez M. Load monitoring for active control of wind turbines. *Renewable and Sustainable Energy Reviews* 2015; **41**:189–201.
26. Larsen TJ, Madsen HA, Thomsen K. Active load reduction using individual pitch, based on local blade flow measurements. *Wind Energy* 2005; **8**(1):67–80.
27. Thomsen SC, Niemann H, Poulsen NK. Individual pitch control of wind turbines using local inflow measurements. *IFAC Proceedings Volumes* 2008; **41**(2):5587–5592.
28. Madsen HA, Bak C, Paulsen US, Gaunaa M, Sørensen N, Fuglsang P, Romblad J, Olsen N, Enevoldsen P, Laursen J, *et al.*. The DAN-AERO MW Experiments. *Conference Proceedings—48th AIAA Aerospace Sciences Meeting Including The New Horizons Forum and Aerospace Exposition*, 2010.
29. Mirzaei M, Henriksen LC, Poulsen NK, Niemann HH, Hansen MH. Individual Pitch Control Using LIDAR Measurements. *IEEE International Conference on Control Applications*, October, 2012; 1646–1651.
30. Mikkelsen T, Angelou N, Hansen K, Sjöholm M, Harris M, Slinger C, Hadley P, Scullion R, Ellis G, Vives G. A spinner-integrated wind lidar for enhanced wind turbine control. *Wind Energy* 2013; **16**(4):625–643.
31. Bottasso C, Pizzinelli P, Riboldi C, Tasca L. LiDAR-enabled model predictive control of wind turbines with real-time capabilities. *Renewable Energy* 2014; **71**:442–452.
32. Scholbrock A, Fleming P, Schlipf D, Wright A, Johnson K, Wang N. Lidar-enhanced wind turbine control: Past, present, and future. *American Control Conference (ACC), 2016*, American Automatic Control Council (AACC), 2016; 1399–1406.
33. Bos R, Giyanani A, Bierbooms W. Assessing the severity of wind gusts with lidar. *Remote Sensing* 2016; **8**(9):758.
34. Towers P, Jones BL. Real-time wind field reconstruction from LiDAR measurements using a dynamic wind model and state estimation. *Wind Energy* 2014; doi:10.1002/we.
35. Churchfield MJ, Lee S, Michalakes J, Moriarty PJ. A numerical study of the effects of atmospheric and wake turbulence on wind turbine dynamics. *Journal of turbulence* 2012; **13**(14):1–32.
36. Kragh KA, Hansen MH, Henriksen LC. Sensor comparison study for load alleviating wind turbine pitch control. *Wind Energy* 2014; **17**(12):1891–1904.
37. Jonkman J, Butterfield S, Musial W, Scott G. Definition of a 5-MW Reference Wind Turbine for Offshore System Development. *Technical Report*, NREL 2009.
38. Aström KJ, Murray RM. *Feedback systems: an introduction for scientists and engineers*. Princeton university press, 2010.
39. Skogestad S, Postlethwaite I. *Multivariable feedback control: analysis and design*, vol. 2. Wiley New York, 2007.
40. McFarlane D, Glover K. A loop-shaping design procedure using H_∞ synthesis. *IEEE transactions on automatic control* 1992; **37**(6):759–769.
41. Jonkman J, Buhl Jr M. FAST user's guide. *Golden, CO: National Renewable Energy Laboratory* 2005; .
42. Jonkman BJ. Turbsim user's guide: Version 1.50. *Technical Report*, National Renewable Energy Laboratory Golden, Colorado 2009.
43. Sutherland JH. On the fatigue analysis of wind turbines. *Technical Report*, Sandia National Labs., Albuquerque, NM (US); Sandia National Labs., Livermore, CA (US) 1999.
44. Niesłony A. Determination of fragments of multiaxial service loading strongly influencing the fatigue of machine components. *Mechanical Systems and Signal Processing* 2009; **23**(8):2712–2721.

DOI: 10.1002/we
Prepared using weauth.cls